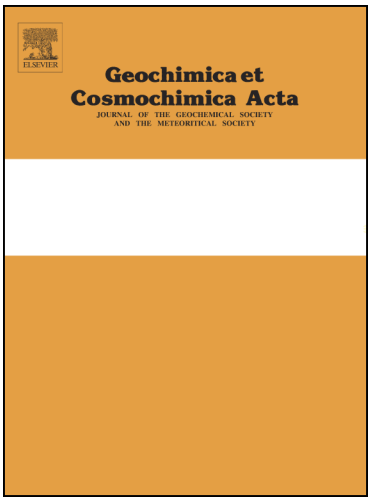

Helium diffusion parameters of hematite from a single-diffusion-domain crystal

K.A. Farley

PII: S0016-7037(18)30200-X
DOI: https://doi.org/10.1016/j.gca.2018.04.005
Reference: GCA 10726

To appear in: *Geochimica et Cosmochimica Acta*

Received Date: 17 December 2017
Accepted Date: 5 April 2018

Please cite this article as: Farley, K.A., Helium diffusion parameters of hematite from a single-diffusion-domain crystal, *Geochimica et Cosmochimica Acta* (2018), doi: https://doi.org/10.1016/j.gca.2018.04.005

Helium diffusion parameters of hematite from a single-diffusion-domain crystal

K.A. Farley

Division of Geological and Planetary Sciences, Caltech, MS 170-25, Pasadena, CA 91125; farley@gps.caltech.edu

Abstract

This contribution reports new parameters for helium diffusion in hematite useful for interpretation of cosmogenic ^{3}He and radiogenic ^{4}He chronometry. Fragments of a coarse, euhedral single crystal of hematite from Minas Gerais, Brazil were subjected to bulk step-heating helium diffusion experiments after proton irradiation to make a uniform distribution of ^{3}He. Aliquots of three different grain sizes ranging from ~300 to ~700 μm in equivalent-sphere radius yielded helium diffusion activation energies E_a~170 kJ/mol, very similar to previous estimates for E_a in hematite. Uniquely in this specimen, diffusivity varies with the dimensions of the analyzed fragments in precisely the fashion expected if the diffusion domain corresponds to the physical grain. This contrasts with previous studies that concluded that the analyzed hematites consist of polycrystalline aggregates in which helium migration is governed by the size distribution of the constituent crystallites. These new data permit a direct estimate of the helium diffusivity at infinite temperature for hematite of $\ln(D_o) = -0.66 \pm 0.35$ cm^2/sec.

The major implication of the new diffusion parameters is that hematite is very retentive of helium even at very small crystal sizes. For example, a 20 nm radius hematite crystal, at the smallest end of the size range so far described in dated polycrystalline hematite specimens, will retain more than 99% of its ingrown He over 1 Myr at 30°C, and more than 90% over 100 Myr. Under most conditions, hematite is close to quantitatively helium-retentive on the Earth's surface, simplifying radiogenic and cosmogenic helium dating of this phase. In a system cooling at 10°C/Myr, the 20 nm hematite crystal has a He closure temperature of ~70°C, similar to a typical ~100 μm apatite crystal.

Helium is likely held tightly in hematite owing to its dense hexagonal closest packing structure and absence of migration-enhancing channels. The isostructural minerals corundum and sapphire are likely to be similarly helium retentive.

1. Introduction

Hematite is increasingly a target for He-based dating using either radiogenic ^{4}He or cosmogenic ^{3}He. For example, (U-Th)/He dating has been used to establish the timing of oxide cap hematite formation in a copper porphyry deposit (Cooper et al., 2016), to constrain the age of faulting using hematite-mineralized fault surfaces (Ault et al., 2015), and to date iron oxide deposition during hydrothermal fluid flow (Evenson et al., 2014). By combining (U-Th)/He dating with ^{4}He/^{3}He

thermochronometry (Shuster and Farley, 2004) and (U-Th)/^{21}Ne dating, hematite has also been used to establish multi-hundred Myr cooling histories spanning ~250°C to surface conditions (Farley and Flowers, 2012). In addition, high concentrations of ^{3}He in hematites in banded iron formations have been used to determine the cosmogenic ^{3}He production rate in this phase, and to demonstrate very slow landscape evolution in parts of tropical Brazil (Shuster et al., 2012).

Accurate knowledge of He diffusion behavior is critical for successful application of He-based chronometry (Farley, 2002). Although early studies showed that hematite is quite retentive of He (Bahr et al., 1994), it has proven difficult to establish the fundamental diffusion parameters that allow a quantitative prediction of diffusive He loss in the diversity of natural situations in which hematite crystal size and/or temperature can vary. This difficulty arises because hematites previously studied for He diffusivity were polycrystalline aggregates, or show clear diffusion-based evidence of being polycrystalline. In well-studied minerals such as apatite and titanite, the He diffusion rate from a sample is governed by the physical dimensions of the analyzed crystal (Reiners and Farley, 1999; Farley, 2000). In contrast, in polycrystalline hematite aggregates, varying the dimensions of the aggregate does not change the He release behavior (Farley and Flowers, 2012). This observation motivates the hypothesis that individual crystallites govern diffusion rate, with fast pathways along crystallite boundaries. Mathematically, such a system can be described by the multiple diffusion domain (MDD) model developed for diffusion of Ar from intra-crystalline structures within some K-feldspars (Lovera et al., 1991), but is here referred to as a poly-crystalline domain (PCD) model to emphasize that the domains are physically recognizable crystallites.

Hematite crystal sizes in nature are extremely variable, ranging from as small as a few nm in red pigments (e.g., in lateritic soils) to cm-size in specular hematite and some large single crystals. The difference in He diffusivity across this size range is expected to be greater than a factor of 10^{8}, clearly consequential for He retentivity under many natural circumstances. From a practical perspective, PCD behavior complicates determination of the He diffusion coefficient and its temperature dependence because multiple crystallite sizes within the aggregate are inevitably diffusing simultaneously during a diffusion experiment. Attempts have been made to overcome this complication by mapping He diffusion behavior to the microscopically observed crystallite size distribution (Farley and Flowers, 2012; Evenson et al., 2014; Farley and McKeon, 2015). However, this approach is fraught with uncertainty, e.g., in determining the full spectrum of crystallite sizes from limited observations usually restricted to two dimensions, and possible size reduction during sample preparation for microscopy. As an alternative approach, density functional theory has been used to model helium diffusivity (Balout et al., 2017), with results generally consistent with experimental measurements.

This paper presents He diffusion data on an unusual single-crystal hematite that exhibits single domain He diffusivity. The results permit direct determination of the diffusivity at infinite temperature (D_o) in hematite, and enable prediction of the He

diffusion behavior of any size hematite crystal or aggregate in which the crystallite size distribution has been estimated. It also permits assessment of He retentivity at a specific temperature, for example at Earth surface conditions. A key conclusion of this work is that He is expected to be retained even in sub-micron sized hematite at Earth surface conditions.

1.1 He Diffusion Background

This section describes the observations that support the PCD model of He in hematite, and describes the difficulty in establishing fundamental diffusion parameters from previous experiments on polycrystalline aggregates.

In thermally activated diffusion, the diffusivity (D) obeys an Arrhenius relationship:

$$D=D_o e^{-Ea/RT} \quad (1)$$

where D_o is the diffusivity at infinite temperature (cm^2/s), E_a is the activation energy (kJ/mol), R is the gas constant, and T is the Kelvin temperature. For some diffusant species, it is possible to measure D and E_a by constructing a known concentration profile and assessing its evolution through time under given boundary conditions and temperature. While this technique is sometimes used for He diffusivity measurements in minerals (e.g., Cherniak et al., 2009), a more sensitive, analytically simpler, and more widely adopted technique is to subject a bulk mineral specimen to a step-heating experiment in which the amount of He released into a vacuum chamber is measured in a series of steps that sequentially degas the sample. Casually referred to as a diffusion coefficient measurement, the quantity derived from such experiments is actually the diffusion coefficient normalized to the square of the characteristic distance the diffusant must traverse to escape the specimen, also called the diffusion domain (a, in cm). This normalized quantity is termed the frequency factor (D/a^2, in units of s^{-1}). For several minerals important for He studies (e.g., apatite, titanite), varying the size of the specimen being analyzed shifts the frequency factor exactly as anticipated if the diffusion domain is the crystal itself, i.e., He diffuses through the entire crystal before being liberated (Reiners and Farley, 1999; Farley, 2000).

In a mineral in which helium obeys thermally activated volume diffusion from a single diffusion domain, equation 1 for a bulk-sample step-heating experiment becomes

$$D/a^2=D_o/a^2 e^{-Ea/RT} \quad (2)$$

Figure 1 shows typical Arrhenius plots for step-heating He release experiments from two different grain sizes of apatite (from Farley et al., 2000). Throughout these experiments, the data for each grain size define a single array consistent with equation 2, and the arrays are vertically offset as expected if the domain radius a is equivalent to the radius of the analyzed grains. In this case, the two fundamental

diffusion parameters, E_a and $D_{o,}$ can both be extracted from the experiments, permitting prediction of He diffusion behavior for any grain size and any temperature.

Figure 1 also shows typical step-heat He measurements obtained on polycrystalline hematite, in this case a sample from a banded iron formation in Michigan (sample MI43 from Farley and McKeon, 2015). These data clearly violate expectations from equation 2 in that they do not define a single linear array, but rather a zig-zag pattern in which diffusivity at a given temperature declines as the experiment proceeds. This is precisely the behavior expected for simultaneous diffusion from a range of domain sizes (Farley and Flowers, 2012). As expected for a poly-domain system, varying the dimensions of the analyzed hematite specimen does not change the diffusion results unless the specimen is ground extremely finely such that the largest crystallites are reduced in size. From an Arrhenius pattern like the hematite in Figure 2, there is no way to isolate D_o from a^2. Although the diffusion behavior of the analyzed specimen can be fully characterized, the experiment offers no straightforward way to predict He diffusion behavior for a different specimen with a potentially different crystallite size or distribution of sizes.

The distinctive behavior of hematite in Figure 1 can be quantitatively understood by considering a system that consists of multiple crystallites (n=1…N) of different characteristic size (a_n) all starting with the same uniform concentration of diffusant (e.g., provided by proton-induced ^{3}He (Shuster and Farley, 2005)) and that are step-heated together. Each crystallite has an associated volume fraction V_n of the total sample, which together with the domain sizes is termed the domain size distribution. Intra-crystalline space is assumed to provide an infinitely fast pathway for He migration.

Each crystallite n will diffuse He independently and will obey the incremental fractional release equation (Fechtig and Kalbitzer, 1966) in each heating step i:

$$F_{n,i} = \boldsymbol{f}(D_o/a_n^2, E_a, t_i, T_i, {}^cF_{n,i-1}) \qquad (3)$$

where $\boldsymbol{f}$ is a known function that depends on domain geometry, t is the step duration, and T the Kelvin temperature. The term ${}^cF_{n,i-1}$ is the cumulative yield for all steps from 1 to i-1 and appears in equation 2 because the incremental fractional yield is strongly dependent on the concentration gradient, which is in turn a function of how much diffusant has been removed prior to the step.

The incremental fractional yield of the entire system in each step i is the volume-weighted sum over the N crystallites:

$$F_i = \Sigma V_n F_{i,n} \qquad (4)$$

Equation 4 describes He loss from a polycrystalline specimen that would be obtained in a step-heating experiment. In the absence of knowledge of the domain

size distribution, data of this type generated experimentally are routinely converted into diffusivity assuming, correctly or not, a single domain size. Specifically, apparent diffusivity (more correctly, frequency factor) in step i is calculated from the entire system's fractional yield and the duration of the step:

$$D_{i,T}/a^2 = \boldsymbol{g}(F_i, t_i, F_{i-1}) \qquad (5)$$

Where $\boldsymbol{g}$ is again a function of domain geometry (Fechtig and Kalbitzer, 1966). The term *apparent* diffusivity is used here to emphasize that the computed quantity ($D_{i,T}/a^2$) for the PCD system is a mathematical construct rather than a reflection of the true diffusivity of any of the individual crystallites that make up the polycrystalline aggregate.

1.2 Isothermal Step-Heat Example

Behavior of these equations during a simulated step-heat for an isothermal system consisting of two spheres differing in radius by a factor of 100 is illustrated in Figure 2. In this example the smaller sphere is assumed to comprise 25% of the total volume of the system. It is assumed that the same diffusion parameters (D_o, E_a) apply to both spheres (see caption to Figure 2) and that they carry the same initially uniform concentration of diffusant. Figure 2a plots the cumulative fractional yields from each sphere and for the combined system against the square root of the cumulative holding time. As the experiment proceeds, the smaller sphere releases diffusant much faster than the larger sphere; the fractional diffusant yield from the combined system always lies between that of the smaller and the larger sphere.

Figure 2b shows the evolution of apparent diffusivity (equation 5) over the course of the experiment. Although the diffusivities computed for the two individual spheres remain constant following equation 2 throughout this isothermal experiment, the apparent diffusivity of the combined system declines monotonically by ~6 natural log units. This temporal pattern arises from the evolving relative contribution of diffusant from the two spheres as the fraction of diffusant remaining in them steadily declines.

The linkage between apparent diffusivity and fraction of diffusant extracted can be seen in Figure 2c. Here the apparent diffusivity of the system initially declines fairly slowly with cumulative yield, falls precipitously at ~25% yield, then becomes nearly constant again. This is a direct visualization of the dominant contribution of the smaller sphere to the yield initially, and the transition to dominance by the larger sphere as the smaller sphere becomes exhausted. The steep decline at 25% yield reflects the fact that the smaller sphere makes up 25% of the volume of the total system. Note that the initial apparent diffusivity (at the start of the experiment) is not identical to that of the smaller sphere because the apparent diffusivity is computed from the yield in a given step as a fraction of the total yield from *the system* not from the total yield of the *small sphere alone*.

Importantly, were figure 2C generated by a laboratory experiment involving two spheres of unknown relative size and volume fraction, it alone provides enough information to uniquely determine the volume factions and the frequency factors (D/a^2) for the two spheres. The key observations are the spread in apparent diffusivity and the value of the cumulative yield at the inflection point. In practice, the unknowns could be determined by misfit minimization between the measured fractional yields and those computed iteratively with the forward model described above.

The right hand axis of Figure 2C introduces an additional notation that becomes useful in the next section. By arbitrarily selecting a reference diffusion domain size (a_{ref}), the difference in frequency factor (Δ) of any other domain size (a) at the same temperature can be computed:

$$\Delta = \ln(D/a_{ref}^2)-\ln(D/a^2)=2\ln(a/a_{ref}) \qquad (5)$$

In Figure 2C the smaller sphere was assumed to be the reference domain size, so it plots at zero on the Δ axis, while the larger sphere (with 100 times larger radius) plots at $2\ln(100)=9.21$ ln units. For comparison to MDD model notation, Δ is just twice the quantity $\ln(r/r_o)$ (Lovera et al., 1991).

1.2 Non-Isothermal Step-Heat Examples

In the previous section the system of two spheres was assumed to be isothermal. Under this restriction it is impossible to determine the diffusion activation energy (E_a, equation 1). Figure 3 shows results of relaxing this restriction: the step heat has varying temperatures, but was computed in exactly the same way as the isothermal case. This plot shows the frequency factors of the two spheres as broad gray lines, parallel to each other (same E_a) and offset from each other by $\Delta = 9.21$ ln units. Model heating schedules include two isothermal experiments (250°C and 450°C), a purely prograde and a purely retrograde experiment, and an experiment that was thermally cycled.

Each of these schedules yields a different evolution of the apparent diffusivity for the system. However, all conform to the observation that the apparent diffusivity declines relative to predictions from a single domain size as the experiment proceeds, just as in the measured Arrhenius plot for polycrystalline hematite (Figure 1). As illustrated by the isothermal experiment in the previous section, this effect arises from the evolving relative contributions of diffusant from each of the two spheres. To make this point more obvious, Figure 3 includes contours of equal yield that connect steps in each experiment for ^cF values of 1, 10, 25, 30, 50, and 90%. Two important observations are evident in this plot: 1) the yield contours are parallel to each other and to the lines associated with the two individual spheres (i.e., all indicate the same E_a), and 2) the relative spacing between the yield contours varies in this space.

The patterns for each heating schedule in Figure 3 represent a combination of variations caused by the evolving state of the diffusion domains (correlated with the fractional yield ^{c}F), and of temperature-induced variations in diffusion coefficient (related to E_a following equation 1) arising from the different heating schedules modeled. Following equations 2 and 5, the line $\Delta=0$ in Figure 3 tracks the temperature-sensitive diffusivity of the smaller sphere. It therefore offers a convenient reference frame by which to eliminate the effects of temperature. In the ln (D/a2) vs ^{c}F space of Figure 2C, all of these new experiments, regardless of heating schedule, fall on the same curve, and all plot identically to the isothermal experiment described in the previous section. Conceptually, using Δ rotates the data in Figure 3 such that the temperature dependence of diffusivity is eliminated, leaving only domain size distribution effects.

These observations motivate an alternative way to visualize the results: the Arrhenius plot for a system with multiple crystallite sizes can be viewed as part of a three-dimensional space in which the Z-axis is the cumulative fractional yield. Viewed this way, Figure 2C is a slice through the Y-Z plane at a given temperature. The Δ curve in Figure 2c is thus an isothermal cross-section of the curving surface on which any measured point must lie in $\ln(D/a^2)$,$10^4/T$, ^{c}F space. The relative spacing of the contours in Figure 3 is the effect of projection of this surface on to the X-Y plane.

Although Figure 2C can be used to determine the relative size and volume fraction of the domains, it carries no information on diffusion activation energy. Instead, activation energy can be obtained from segments of step heats in which the yield is small, such that the relative proportions of diffusant in the different domains is not changing over the segment. Stated differently, any set of steps over which the yield is vanishingly small must follow a yield contour in Figure 3, i.e., it must define a slope proportional to the activation energy. In practice this is most often accomplished by a retrograde-prograde sequence (red circles in Figure 3) in which the step durations are kept as short as possible consistent with obtaining enough diffusant to make an accurate measurement. The desire to obtain both the domain size distribution and the activation energy leads to step-heating schedules involving multiple prograde-retrograde sequences and produces the characteristic declining zig-zag pattern on a PCD Arrhenius plot. As before, misfit minimization of the fractional yield is used to obtain a best fit solution for E_a and the relative domain size distribution (i.e., the minimization yields D_o/a^2 values, not a values). Also as before, there is no method by which to determine D_o from these data. Although it is tempting to relate the prograde-retrograde sequences that define parallel arrays in Figure 3 to specific crystallite sizes present in the analyzed material (and possibly to the number of different crystallite sizes), this is demonstrably incorrect because these arrays lie nowhere near the arrays defined by the two crystal sizes modeled in this example.

This example considered two crystal sizes, but it could easily be expanded to include more than two. The major observable difference would be an inflection point in Figure 2c for each different size.

2. Samples and Methods

This work describes a hematite specimen in which a) diffusion measurements define a single array in Arrhenius space rather than the declining zig-zag pattern characteristic of PCD diffusion, and 2) varying the dimensions of the specimen varies the measured frequency factor. These data permit determination of D_o, and thus prediction of He diffusion behavior for any crystallite size.

Sample CIT 2048 was selected from the Caltech mineral collection for its well-developed crystal habit, suggesting it might be a single massive crystal (inset to Figure 4). The sample measures ~ 4 cm across and is characterized by well-developed broadly pyramidal crystal faces. The curation document indicates it was collected in Minas Gerais, Brazil. Although the exact source is unknown, very similar euhedral hematite crystals are obtained at the Casa de Pedra iron mine near Congonhas del Campo (20° 28' S, 43° 55' W). The Casa de Pedra deposit is a folded Paleoproterozoic banded iron formation in the Quadrilatero Ferrifero. Low grade regional metamorphism has modified the chemical and structural properties of iron oxides in this region (Mendes and Lagoeiro, 2012).

A ~50 mg chunk of hematite was removed from the original specimen and gently crushed to produce crystal fragments ranging in size from a few tens of um to about 2 mm across. The fragments were washed in water and ethanol to remove adhering fines. In order to produce a uniform distribution of ^{3}He for diffusion studies, the crushed hematite was irradiated for 24 hours with 220 MeV protons at the Francis H. Burr Proton Therapy Center at Massachusetts General Hospital following standard procedures (Shuster and Farley, 2005).

Three size-sorted aliquots of between one and fifteen fragments of the irradiated hematite were subjected to step-heating diffusion experiments. The analyzed grains were selected to be roughly equant. Dimensions were measured under a binocular microscope. Mean equivalent sphere radii (Meesters and Dunai, 2002) are 684, 294, and 425 ums for aliquots D4, D5, and D10, respectively.

Aliquot D10 was a pathfinder experiment used to identify this sample as a candidate for single diffusion domain behavior. It was heated in a copper foil packet using a projector lamp apparatus (Farley et al., 1999) at temperatures <520°C. The remaining two aliquots (D4, D5) were heated in a similar device, but in order to achieve higher temperatures (and thus greater degrees of He extraction) a diode laser was used in place of the projector lamp. To prevent volatilization of the copper foil pouch during high temperature laser heating, the pouch was loaded into an alumina tube, which itself was heated by the laser. Steps were held isothermal for between 15 minutes and 8 hours. In all cases the ramp time was a small fraction of

the hold time at setpoint. Temperature was monitored via a K-type thermocouple, providing closed-loop control of the lamp or laser output. Formal temperature uncertainty was dominated by small (few ^{o}C) oscillations in the feedback loop; it is possible that temperature gradients between sample and thermocouple are larger than this uncertainty estimate. Gradients are more likely for the laser-heated samples than for the lamp-heated sample given the higher temperatures involved, the smaller spot size of the incident radiation, and the alumina tube used to indirectly laser-heat the sample. All three samples were subjected to multiple prograde-retrograde heating cycles to evaluate possible PCD behavior. Sample D10 began with a retrograde sequence, while D4 and D5 both began with a prograde sequence (Table 1). Sample D10 was completely degassed by repeated heating to ~1050^{o}C with the laser. The other two samples were thoroughly degassed by repeated heating to ~1400^{o}C in a resistance furnace.

For D4 and D5, evolved He from each step was sequentially exposed to a pair of SAES NP10 getters operating at ~250^{o}C and room temperature for purification, cryo-focused at 14^{o}K on charcoal, then released from the charcoal at 34^{o}K into a MAP 215-50 mass spectrometer. ^{3}He was measured on a channeltron pulse-counting multiplier, while ^{4}He was measured by magnetic peak-hopping to a Faraday detector. For sample D10, evolved He was similarly purified on a pair of NP-10 getters, but was then admitted directly into a GV Helix-SFT mass spectrometer. ^{3}He was measured on a Pfeiffer SEM 217 discrete dynode multiplier operating in pulse counting mode. Using accelerating voltage hopping, ^{4}He was also measured on the SEM 217.

Steps always yielded very little ^{4}He (<.01 pmol), indicative of a sample nearly devoid of natural radiogenic He (presumably owing to very low U, Th concentration). However, proton-induced ^{3}He was readily measurable, with yields ranging from ~ 5 cps to ~ 10^{4} cps (~10^{-18} to 2x10^{-15} mol). Cold chamber blanks were measured several times during the step-heating of each sample. ^{3}He yields were typically less than 1 cps (~2x10^{-19} mol) and were subtracted from each step. This blank correction was usually negligibly small (<few %) but for some very low yield steps contributed up to 15% of the total measured ^{3}He.

Sensitivity was established from a high ^{3}He/^{4}He ratio standard analyzed on a regular schedule, typically every fifth analysis during the step heating experiments. Pressure linearity was confirmed for the range of ^{4}He signals obtained on samples from the analysis of standards of various sizes before or after each step heat.

Measured ^{3}He for each step was converted into fractional yield from the entire aliquot, combined with the step-heating duration, and translated into an apparent diffusion coefficient using the usual spherical approximation equation (Fechtig and Kalbitzer, 1966).

3. Results

Complete results of the step-heating experiments are shown in Table 1 and plotted as apparent diffusivity in Figure 4. The pathfinder sample D10, heated with the projector lamp apparatus, could only be degassed of 3% of its ^{3}He (maximum temperature 520^{o}C), while laser-heated samples D4 and D5 were degassed of 25% and 72% at temperatures as high as 800-850^{o}C, respectively.

All three samples define fairly consistent linear Arrhenius arrays with the notable exception of the earliest steps. For example, the first few steps of sample D10 plot systematically lower than the rest of the array for this sample. Similarly, the first few steps of samples D4 and D5 plot slightly above the rest of their associated arrays. These early steps comprise less than 1% of the total ^{3}He in the sample, and suggest that the behavior of the most accessible helium in the sample is slightly different from that of the helium carried in the bulk of the sample. A possible explanation for this observation is that surface and/or geometric effects influence the initial He yield. In any case, these anomalous points are indicated in Figure 4 with small symbols, and in the rest of the discussion and plots they are ignored.

The vertical position of the linear arrays of the three aliquots corresponds with the analyzed grain size, with the apparent diffusivity increasing in the order D4 (r=680μm), D10 (r=425 μm), D5 (r=294 μm). All three arrays lie well below the declining zig-zag array of the typical PCD sample from Michigan. Despite these differences, all three aliquots of sample CIT 2048 indicate an activation energy of ~170 kJ/mol, similar to previous results (e.g., Farley and Flowers, 2012).

The straightforward hypothesis for these observations is that the diffusion lengthscale of hematite CIT 2048 is much larger than those in the polycrystalline specimen MI43 (Farley and McKeon, 2014), and corresponds to the dimensions of the crystal fragments analyzed. To test this hypothesis, Figure 5 recasts the apparent diffusivity (D/a^2) into true diffusivity (D) by multiplying by the square of the equivalent sphere radius for each aliquot. In this space the three aliquots plot nearly on top of each other, confirming the correspondence between physical dimension and diffusion domain dimension, thus permitting characterization of D_o. Regression of all of the data in Figure 5 together yields $\ln(D_o) = -0.66 \pm 0.35$ and E_a=171±2.5 kJ/mol with a correlation coefficient r^2 of 0.98.

4. Implications

This section explores the implications of this directly measured D_o value for He diffusion in hematite, assuming it is representative of hematites in general. First, relative domain size distributions reported for polycrystalline hematite samples in previous studies can be converted into crystallite size distributions to determine whether they are plausible. For example, Figure 6 shows expected Arrhenius arrays for single-domain hematites of varying radius. This plot indicates that for the Michigan hematite used as the PCD example in Figure 1, the crystallites range in radius from as large as ~20 μm to as small as a few tens of nm. Similar results are obtained from other published hematites (e.g., in Farley and Flowers, 2012, and

Farley and McKeon, 2015). This size range is reasonable given microscopic examination of the hematites, and supports the general idea that the individual crystallites are acting as diffusion domains.

The first small fraction of He extracted from a sample, inevitably obtained in the early lowest temperature steps, could reside in very tiny domains (crystallite radii of a few nm, comparable to a few unit cells of hematite). Alternatively, this He could be located within the intra-crystalline space in the aggregate; at sufficiently low temperatures it is possible that the intracrystalline region can retain He. Although that possibility would violate the PCD model, this region does not host more than a fraction of a percent of the total ^{3}He in previously analyzed hematites (Farley and Flowers, 2012; Farley and Mckeon, 2015). It is therefore essentially irrelevant for applications of the polycrystalline model for chronometry. Stated differently, caution should be observed when interpreting the initial He yield (<<1%) from a hematite sample in terms of a specific and very tiny domain size.

Based on a compilation of apparent diffusivity data on hematites, Evenson et al. (2014) offered the first published estimate of D_o for hematite of 2.2×10^{-4} cm^2/s. This value is similar to that reported from density functional theory modeling, 9.32×10^{-3} cm^2/s. These values are more than three orders of magnitude smaller than D_o directly measured here. Using these lower D_o values to compute the domain size of CIT 2048 from the apparent diffusivity results in Figure 4 yields radii of a few tens of μm. If the domains were actually that small, than the measured Arrhenius data for the three aliquots, with physical dimensions spanning ~300-700 μm, should be identical to each other because the aliquots would be polycrystalline aggregates rather than single crystals. Furthermore, the aliquots should display the declining zig-zag Arrhenius pattern for the same reason. Since neither is observed, and given the indirect method used by Evenson et al. (2014) and Balout et al. (2017) to infer D_o, the current estimate of D_o=0.5 is likely to be more accurate.

The new diffusion parameters can also be used to characterize He loss in the natural setting. In a system cooling at 10°C/Ma, the He closure temperature of hematite ranges from ~70°C for a 20 nm radius crystallite to 250°C for a crystallite of 1 mm radius (Figure 7). At a comparable grain size, hematite has a far higher closure temperature than apatite, and is at the high end of estimates for titanite and zircon. Although this plot offers a quantitative assessment of the He age expected of a single-domain hematite on a simple cooling path, accurate prediction of He ages of a PCD hematite requires a numerical model that fully incorporates the domain size distribution (Gallagher, 2012; Farley and Flowers, 2012). The domain size distribution is most directly generated by a ^{3}He-based diffusion experiment.

Unlike most phases previously dated with the (U-Th)/He method, hematites are often produced at or near the Earth's surface and remain there for geologically long time periods. Under such conditions it is useful to investigate the fraction of helium retained as a function of crystallite size and isothermal holding time. Based on the diffusion parameters of CIT 2048 and the computational approach of Wolf et al.

(1998), at temperatures as high as 50°C hematite crystallites larger than 1 μm radius will quantitatively (>99%) retain He over a 100 Myr duration. The smallest crystallites revealed by ^{3}He diffusion data in the Michigan sample are about 100 nm in radius. At this size, quantitative retentivity is assured to temperatures as high as 25°C for 100 Myr. Only at crystallite sizes of ~20 nm radius and smaller do loss effects under plausible surface conditions become noticeable: held at 30°C for 100 Myr a 20 nm hematite retains 92% of ingrown He (Figure 8). At the hottest terrestrial localities, such as Death Valley, California, the mean effective diffusion temperature (Tremblay et al. 2014) for He in hematite is ~34°C when considering the full diurnal cycle, and ~48°C when including the additional effects of direct solar heating (using temperature data in Wolf et al., 1998). Even at these extreme effective temperatures hematite crystallites as small as 20 nm retain a very large fraction of ingrown He over multimillion year time scales (Figure 8).

These observations indicate that under common circumstances, the effects of He loss at the Earth's surface can be ignored except for very tiny crystallites of hematite. As an extreme example, the very fine-grained (tens to hundreds of nm) hematite crystals in many soils and cements may be datable with either ^{3}He or ^{4}He if the hematite can be extracted and the consequences of implantation-ejection of ^{3}He or ^{4}He can be quantitatively modeled (Farley et al., 1996; Amidon et al., 2008).

5. Conclusions

In fragments of a coarse, euhedral hematite crystal, He diffusion behaves in a fashion consistent with correspondence between the diffusion domain and the physical dimensions of the analyzed specimen. This is in contrast to previously studied specimens in which He diffusivity is controlled by sub-grain domains, most likely the individual crystallites that make up polycrystalline hematite aggregates. The new data allow determination of the fundamental He diffusion parameters in hematite: $\ln(D_o) = -0.66 \pm 0.35$ (in cm^2/sec) and E_a=171±2.5 kJ/mol.

These hematite He diffusion parameters allow prediction of the behavior of He in hematites of varying crystallite size and under varying temperature conditions, subject to the assumption that the new values are representative of hematites in general. Compared to previously studied phases (apatite, titanite, zircon) at a comparable grain size, hematite is a more He retentive mineral. The hematite structure consists of hexagonally-closest-packed oxygen atoms, with no through-going structural channels; both factors likely impede He migration. This observation is consistent with the DFT study of He diffusion in hematite (Balout et al., 2017). The isostructural minerals ilmenite and corundum are expected to be similarly He retentive.

Acknowledgements
This work was supported by the National Science Foundation, Grant EAR-1144500. Fruitful discussions with Paulo Vasconcelos and helpful reviews by Alexis Ault, Oscar Lovera, and Marissa Tremblay are gratefully acknowledged.

References

Amidon W. H., Farley K. A., Burbank D. W. and Pratt-Sitaula B. (2008) Anomalous cosmogenic He-3 production and elevation scaling in the high Himalaya. *Earth Planet. Sci. Lett.* **265**, 287–301.

Ault A. K., Reiners P. W., Evans J. P. and Thomson S. N. (2015) Linking hematite (U-Th)/He dating with the microtextural record of seismicity in the Wasatch fault damage zone, Utah, USA. *Geology* **43**, 771–774.

Bahr R., Lippolt H. J. and Wernicke R. S. (1994) Temperature-induced 4He degassing of specularite and botryoidal hematite: A 4He retentivity study. *J. Geophys. Res.* **99**, 17,695-17,707.

Balout, H., Roques, J., Gautheron, C., Tassan-Got, L., Mbongo-Djimbi, D., 2017, Helium diffusion in pure hematite (α-Fe2O3) for thermochronometric applications: a theoretical multi-scale study. *Computational and Theoretical Chemistry*, **1099**, 21-28.

Cherniak D. J., Watson E. B. and Thomas J. B. (2009) Diffusion of helium in zircon and apatite. *Chem. Geol.* **268**, 155–166.

Cooper F. J., Adams B. A., Blundy J. D., Farley K. A., McKeon R. E. and Ruggiero A. (2016) Aridity-induced Miocene canyon incision in the Central Andes. *Geology* **44**, 675–678.

Dodson M. H. (1973) Closure temperatures in cooling geological and petrological systems. *Contrib. Mineral. Petrol.* **40**, 259–274.

Evenson N. S., Reiners P. W., Spencer J. E. and Shuster D. L. (2014) Hematite and Mn oxide (U-Th)/He dates from the Buckskin-Rawhide detachment system, western Arizona: gaining insights into hematite (U-Th)/He systematics. *Am. J. Sci.* **314**, 1373–1435.

Farley K. A. (2000) Helium diffusion from apatite: General behavior as illustrated by Durango fluorapatite. *J. Geophys. Res.-Solid Earth* **105**, 2903–2914.

Farley K. A. (2002) (U-Th)/He dating: Techniques, calibrations, and applications. In *Reviews In Mineralogy & Geochemistry Volume 47*. Washington. pp. 819–844.

Farley K. A. and Flowers R. M. (2012) (U-Th)/Ne and multidomain (U-Th)/He systematics of a hydrothermal hematite from eastern Grand Canyon. *Earth Planet. Sci. Lett.* **359**, 131–140.

Farley K. A. and McKeon R. (2015) Radiometric dating and temperature history of banded iron formation–associated hematite, Gogebic iron range, Michigan, USA. *Geology* **43**, 1083–1086.

Farley K. A., Reiners P. W. and Nenow V. (1999) An apparatus for high-precision helium diffusion measurements from minerals. *Anal. Chem.* **71**, 2059–2061.

Farley K. A., Wolf R. A. and Silver L. T. (1996) The effects of long alpha-stopping distances on (U-Th)/He ages. *Geochim. Cosmochim. Acta* **60**, 4223–4229.

Fechtig H. and Kalbitzer S. (1966) The diffusion of argon in potassium-bearing solids. In *Potassium Argon Dating* (eds. O. A. Schaeffer and J. Zahringer). Springer Verlag, New York.

Gallagher K. (2012) Transdimensional inverse thermal history modeling for quantitative thermochronology. *J. Geophys. Res.-Solid Earth* **117**.

Lovera O. M., Richter F. M. and Harrison T. M. (1991) Diffusion domains determined by 39Ar released during step heating. *J. Geophys. Res.* **96**, 2057–2069.

Meesters A. G. C. A. and Dunai T. J. (2002) Solving the production- diffusion equation for finite diffusion domains of various shapes, part 1; implications for low temperature (U-Th)/He thermochronology. *Chem. Geol.* **186**, 333-344.

Mendes M. and Lagoeiro L. (2012) Microstructures, crystallographic fabric development and deformation mechanisms in natural hematite aggregates deformed under varied metamorphic conditions. *J. Struct. Geol.* **40**, 29–43.

Reiners P. W. and Farley K. A. (1999) Helium diffusion and (U-Th)/He thermochronometry of titanite. *Geochim. Cosmochim. Acta* **63**, 3845–3859.

Shuster D. L. and Farley K. A. (2005) Diffusion kinetics of proton-induced Ne-21, He-3, and He-4 in quartz. *Geochim. Cosmochim. Acta* **69**, 2349–2359.

Shuster D. L. and Farley K. A. (2004) He-4/He-3 thermochronometry. *Earth Planet. Sci. Lett.* **217**, 1–17.

Shuster D. L., Farley K. A., Vasconcelos P. M., Balco G., Monteiro H. S., Waltenberg K. and Stone J. O. (2012) Cosmogenic He-3 in hematite and goethite from Brazilian "canga" duricrust demonstrates the extreme stability of these surfaces. *Earth Planet. Sci. Lett.* **329**, 41–50.

Tremblay, M.M., Shuster, D.L., and Balco, G., 2014, Cosmogenic noble gas paleothermometry. *Earth and Planet. Sci. Lett*, **400**, 195-205.

Wolf R. A., Farley K. A. and Kass D. M. (1998) Modeling of the temperature sensitivity of the apatite (U-Th)/He thermochronometer. *Chem. Geol.* **148**, 105–114.

Figure Captions

Figure 1. Comparison of published He diffusion data from apatite (red points, Durango apatite from Farley, 2000) and from a polycrystalline aggregate hematite from Michigan (MI43-2, Farley and McKeon, 2015). The apatite data define arrays for each grain size throughout the degassing of the sample, and the vertical offset between the arrays is consistent with correspondence between He diffusion domain radius and physical grain dimensions. In contrast, the hematite results define a zig-zag pattern of ever-decreasing diffusivity at a given temperature as the experiment proceeds. In addition, analyses of aliquots of MI43 of different equivalent sphere radius do not change the He diffusion results (not shown).

Figure 2. Simulation of results expected from equations 2-5 for a system consisting of two spheres differing in size by a factor of 100 with the smaller sphere making up 25% of the volume of the system. A) shows that the smaller sphere loses diffusant much faster than the larger sphere, and the combined system is intermediate in behavior and with a notable break in slope when the small domain is exhausted of diffusant. B) Apparent diffusivity for the two individual spheres is invariant in this isothermal experiment, but the apparent diffusivity for the combined system declines monotonically as the dominant source of diffusant switches from the small sphere to the large sphere when the small sphere becomes exhausted. Δ denotes the vertical offset between the apparent diffusivity of the small sphere and the apparent diffusivity of either sphere or the combined system (equation 5). C) Δ for the two spheres is constant throughout the experiment reflecting the different assumed radii, but for the combined system, Δ increases dramatically at the cumulative yield corresponding to the volume fraction of the small sphere as it becomes exhausted of diffusant. The vertical lines correspond to fractional yields also indicated on Figure 3 (1, 10, 25, 30, 50, and 90%). For this illustration and that in Figure 3, an activation energy appropriate for hematite, E_a=157 kJ/mol, was assumed (Farley and Flowers, 2014; Balout et al.; 2017). $\ln(D_o/a^2)$ values for the two spheres of 27.6 and 18.4 were also assumed.

Figure 3. Apparent diffusivity in the model two-sphere system with five different heating schedules. All demonstrate the characteristic of PCD diffusion: the diffusivity at a given temperature declines as the experiment proceeds. Small arrows indicate order of data points collected in each step-heating experiment. The thick gray lines indicate the diffusivities of the two individual spheres. The parallel dotted lines are contours of cumulative fractional yield applicable to every heating schedule, with % yield indicated (1, 10, 25, 30, 50, and 90%). For illustration, Δ is indicated for two different data points, as the vertical offset from the indicated Δ=0 line.

Figure 4. Apparent He diffusion (D/a^2) Arrhenius plot for the three aliquots of sample CIT 2048 hematite (original sample pictured in upper right, largest crystal is 4 cm across) and the PCD sample MI-43 (total specimen length is 17 cm). Equivalent

sphere radii are indicated in legend. Although somewhat scattered, the three aliquots yield consistent linear arrays, the position of which correlates with the dimensions of the analyzed grain. Note that all three aliquots are much more retentive than the polycrystalline Michigan sample. Smaller symbols indicate early steps corresponding to less than 1% cumulative yield.

Figure 5. He diffusion (D) Arrhenius plot computed by multiplying measured frequency factor by the square of the equivalent sphere radius of each aliquot. Symbols are the same as in Figure 4. The fact that the three arrays seen in Figure 4 converge to a single array here indicates that the diffusion domain in CIT 2048 is the physical grain. Linear regression of all data in this plot indicates $\ln(D_o) = -0.66 \pm 0.35$ (cm^2/s)and E_a=171±2.5 kJ/mol. As described in the text, the first few data points of each of the runs were excluded from the computation and plot.

Figure 6. Apparent He diffusion (D/a^2) Arrhenius plot with contours indicating domain size based on the D_o value derived from CIT 2048 data in Figure 5. Symbols are the same as in Figure 4. The polycrystalline Michigan hematite is predicted to have domain sizes ranging from 20 μm to a few tens of nm. This size range is in reasonable agreement with microscopic observations of the sample (Farley and McKeon, 2015).

Figure 7. He closure temperature for hematite crystals of varying size. This curve was computed from the best-fit parameters in Figure 5 ($\ln(D_o) = -0.66 \pm 0.35$ and E_a=171±2.5 kJ/mol) and the closure temperature model of Dodson (1973).

Figure 8. Fractional retention of radiogenic or cosmogenic He produced in a hematite of r=0.02 μm as a function of hold time for several different temperatures. Even over periods of tens of Myr and temperatures up to 35°C, ingrown He is very strongly retained even in this small grain size. The curves were computed using the diffusion parameters from Figure 5 and the computational approach described by Wolf et al. (1998).

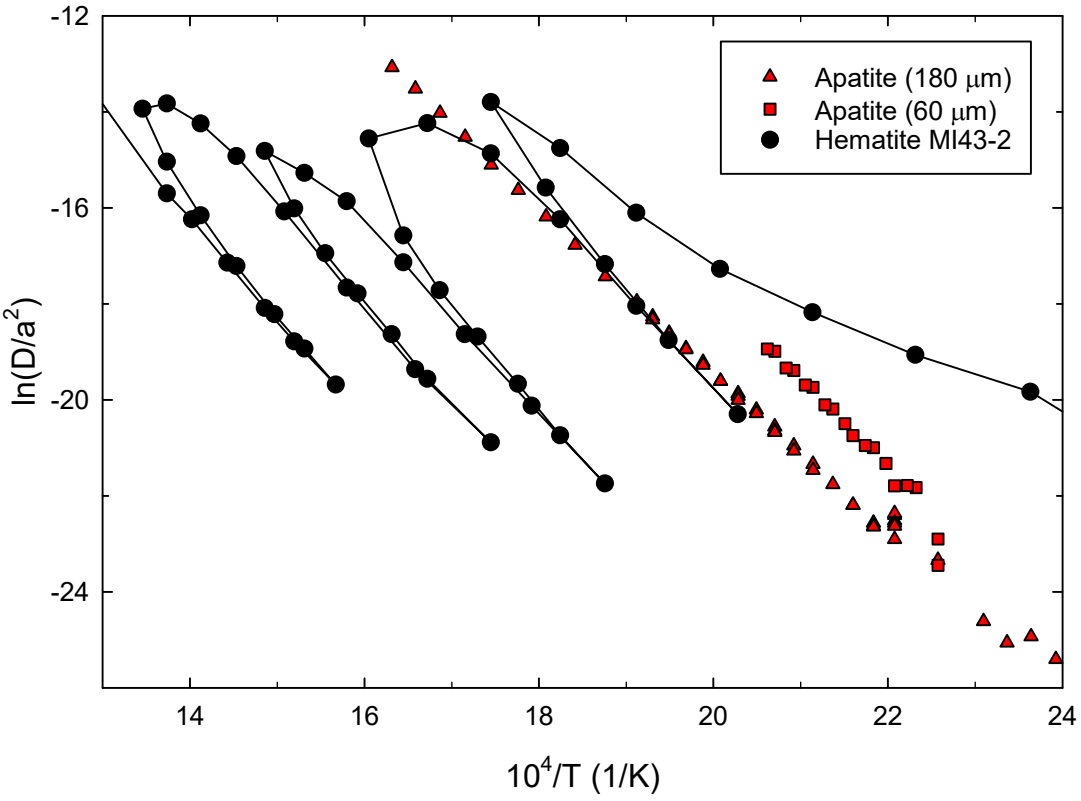
-12
-16
-20
-24
ln(D/a^2)
14
16
18
20
22
24
10^4/T (1/K)
Apatite (180 μm)
Apatite (60 μm)
Hematite MI43-2

Figure 1

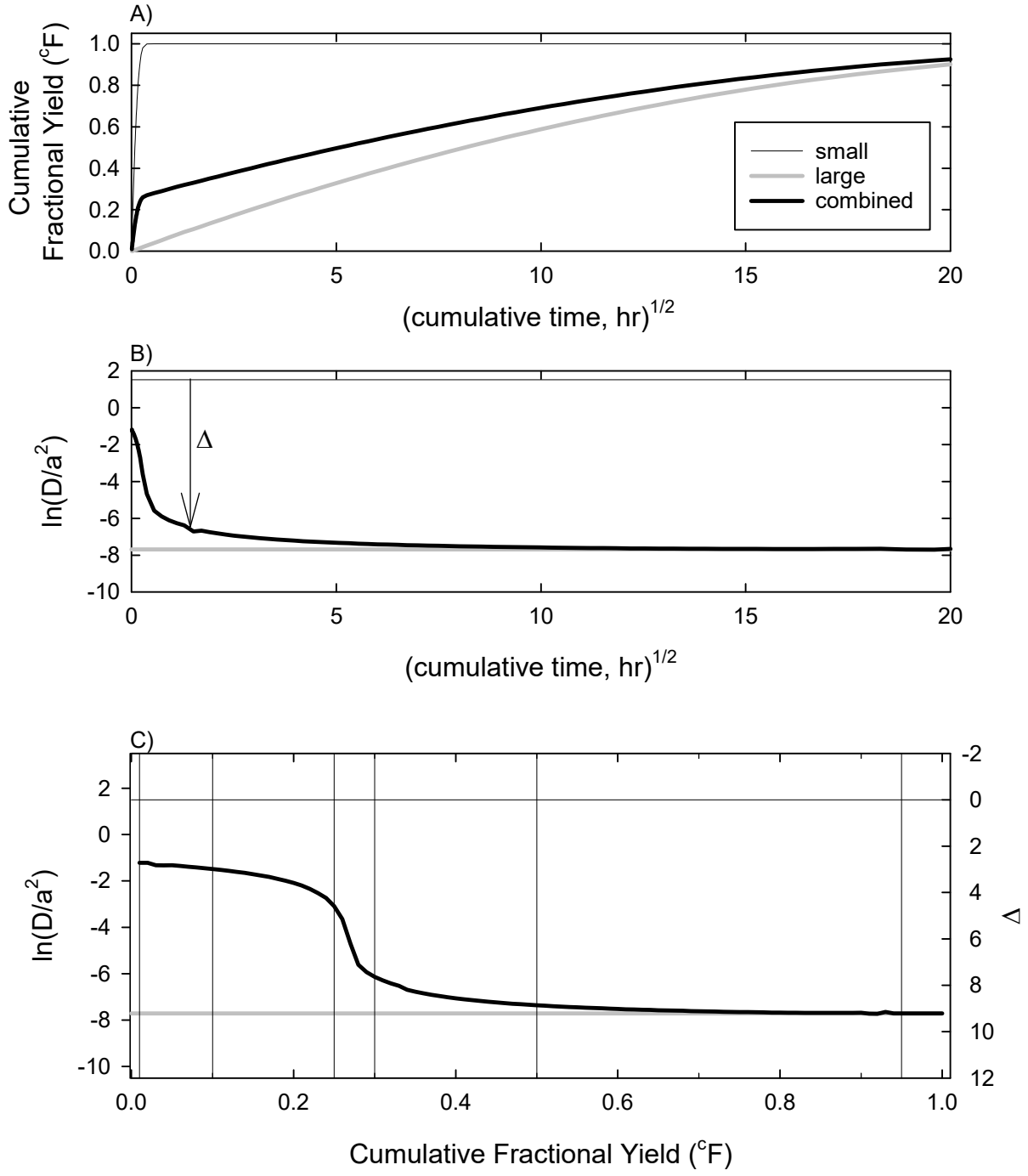
A)
Cumulative Fractional Yield (^{c}F)
1.0
0.8
0.6
0.4
0.2
0.0
0
5
10
15
20
small
large
combined
(cumulative time, hr)$^{1/2}$
B)
ln(D/a^2)
2
0
-2
-4
-6
-8
-10
Δ
0
5
10
15
20
(cumulative time, hr)$^{1/2}$
C)
ln(D/a^2)
2
0
-2
-4
-6
-8
-10
-2
0
2
4
6
8
10
12
Δ
0.0
0.2
0.4
0.6
0.8
1.0
Cumulative Fractional Yield (^{c}F)

Figure 2

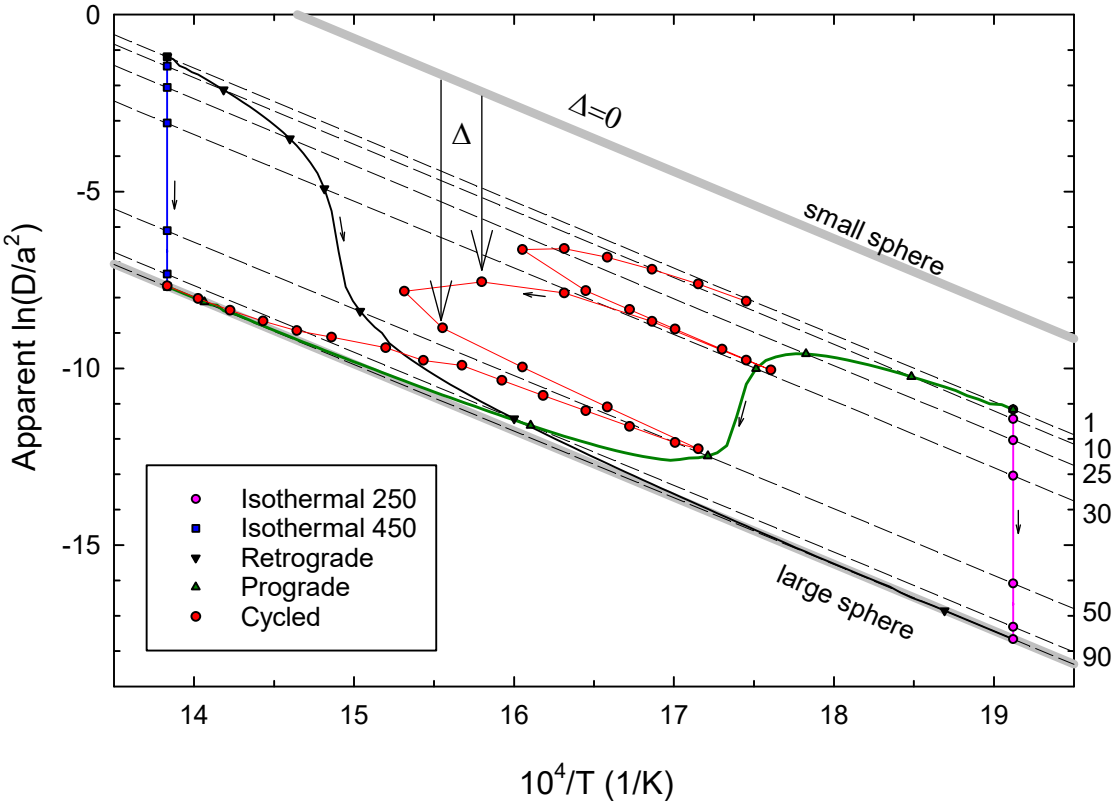
0
-5
-10
-15
Apparent ln(D/a^2)
14
15
16
17
18
19
10^4/T (1/K)
Δ
Δ=0
small sphere
large sphere
1
10
25
30
50
90
Isothermal 250
Isothermal 450
Retrograde
Prograde
Cycled

Figure 3

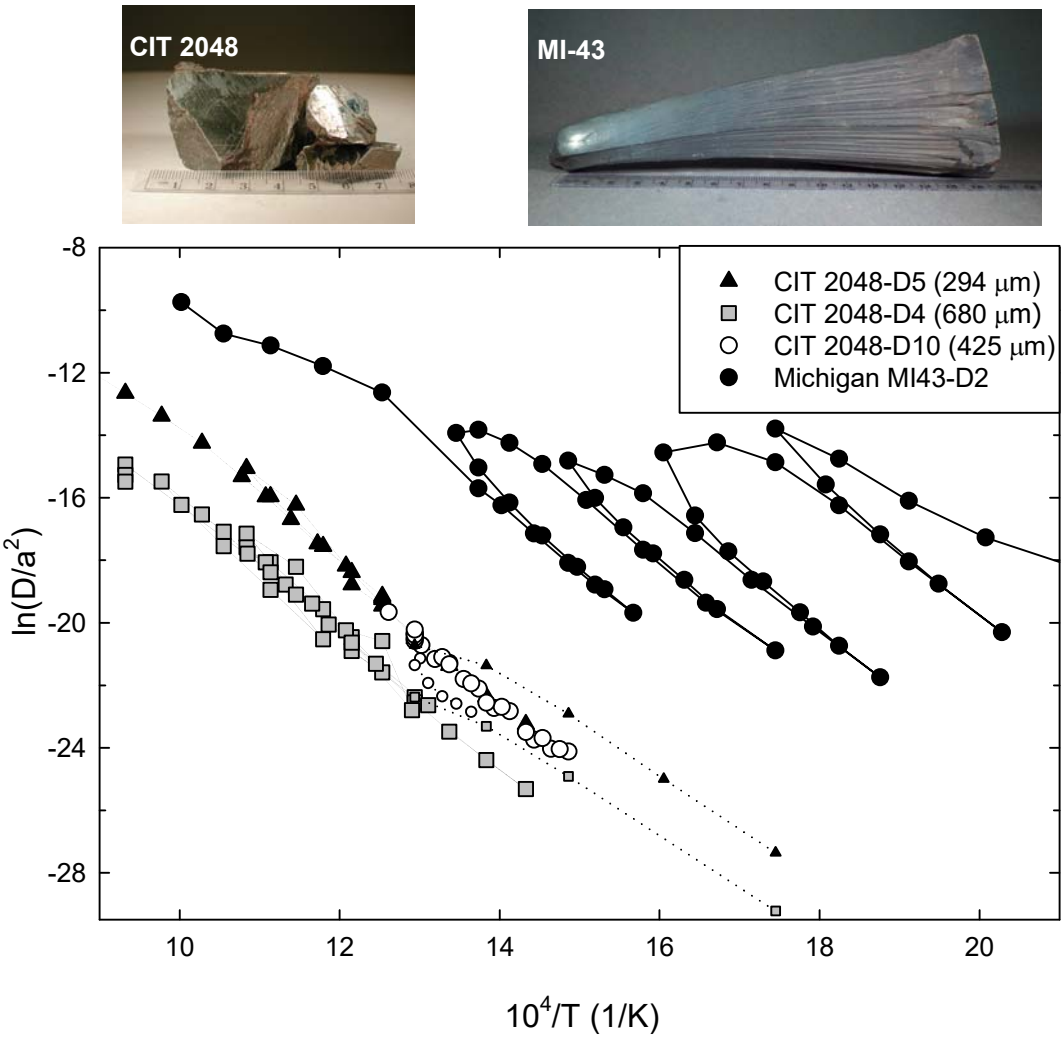
CIT 2048
MI-43
CIT 2048-D5 (294 μm)
CIT 2048-D4 (680 μm)
CIT 2048-D10 (425 μm)
Michigan MI43-D2
ln(D/a²)
-8
-12
-16
-20
-24
-28
10
12
14
16
18
20
10⁴/T (1/K)

Figure 4

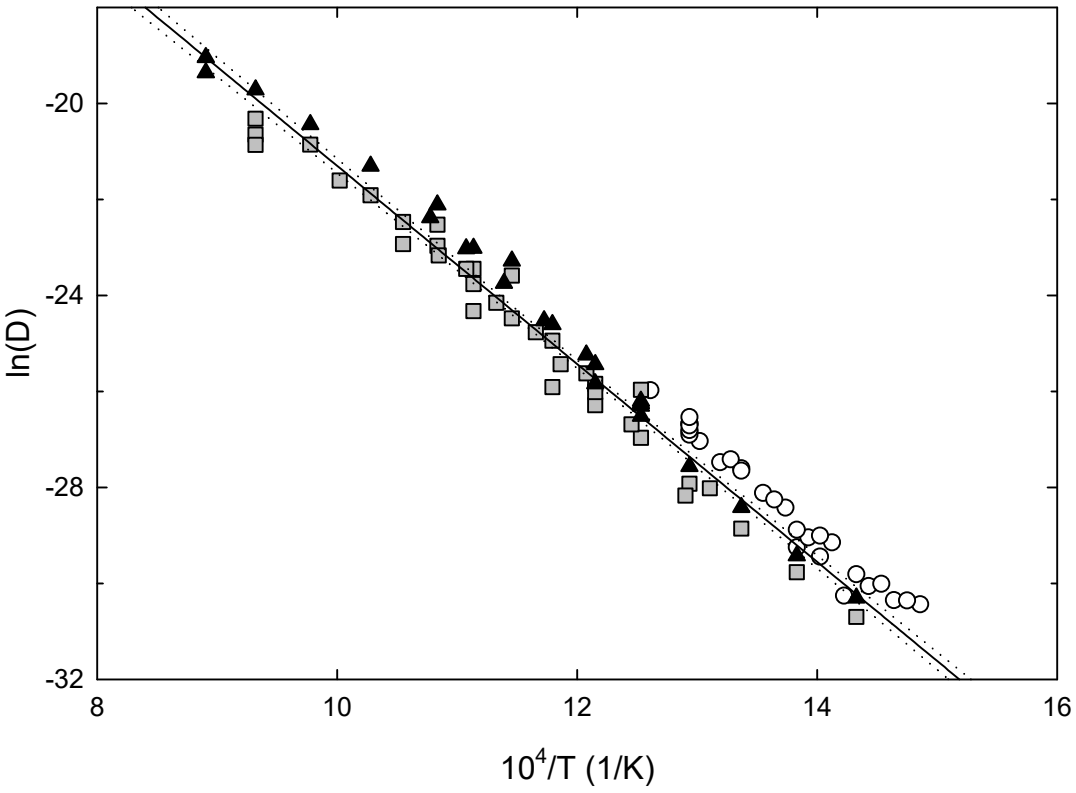

Figure 5

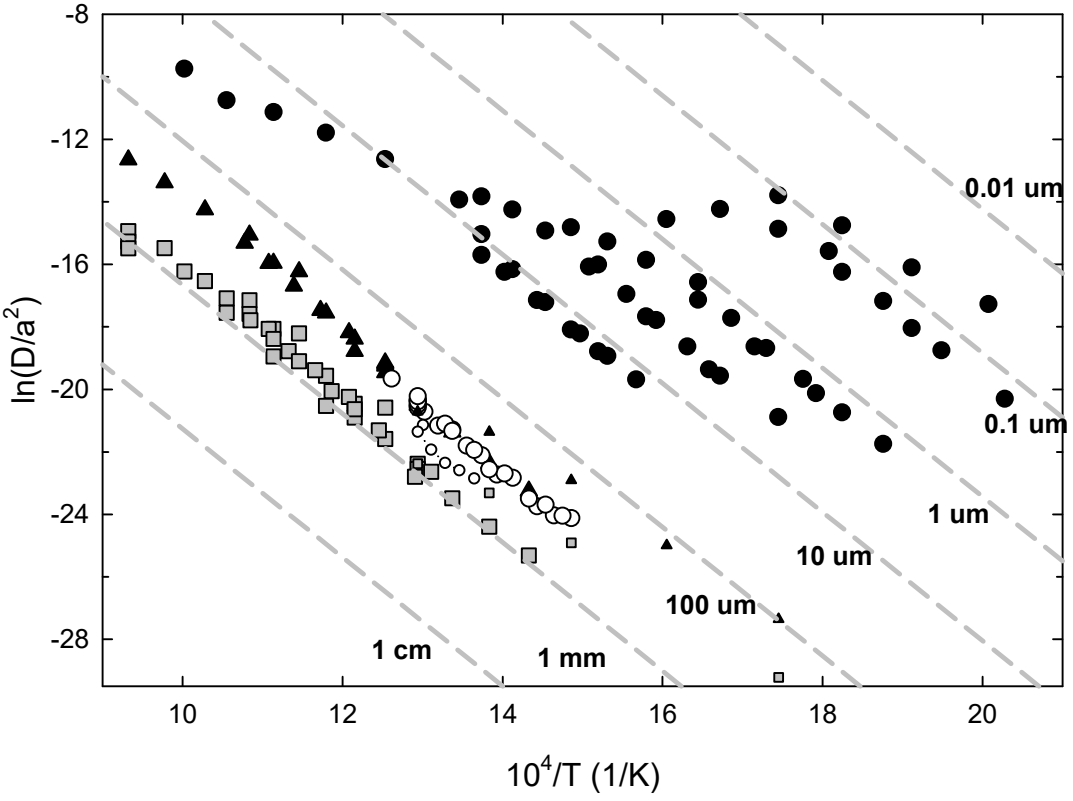
-8
-12
-16
-20
-24
-28
ln(D/a^2)
10
12
14
16
18
20
10^4/T (1/K)
0.01 um
0.1 um
1 um
10 um
100 um
1 mm
1 cm

Figure 6

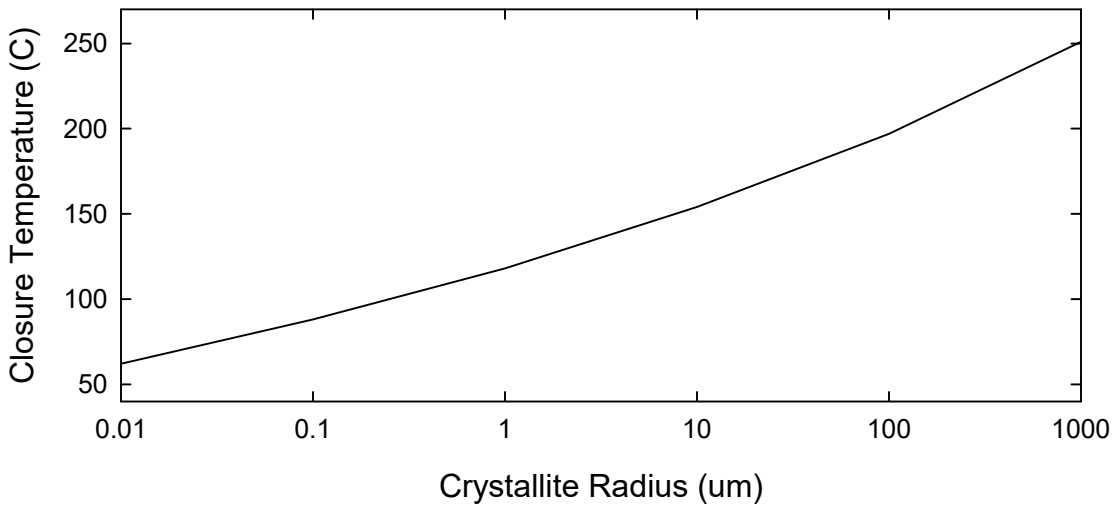
Closure Temperature (C)
250
200
150
100
50
0.01
0.1
1
10
100
1000
Crystallite Radius (um)

Figure 7

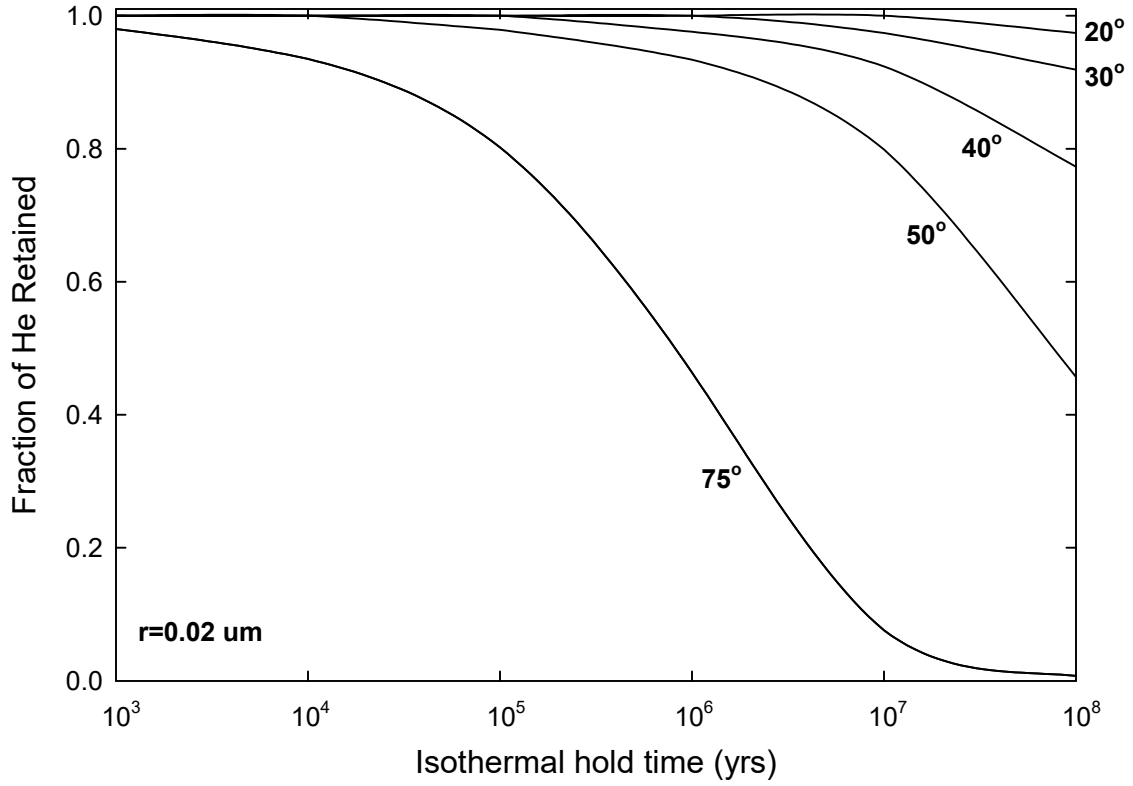
1.0
0.8
0.6
0.4
0.2
0.0
Fraction of He Retained
10^3
10^4
10^5
10^6
10^7
10^8
Isothermal hold time (yrs)
20°
30°
40°
50°
75°
r=0.02 um

Figure 8

Table 1 - He Diffusion data from CIT-2048

CIT-2048 D4
Equivalent sphere radius of 680 µm

Temp (C)	Time (hr)	^{3}He (10^{-18} mol)	± σ	^{C}F	ln(D/a^2)	ln(D)
300	1.03	1.297	0.0389	0.0001	-29.22	-34.59
400	1.02	9.869	0.2961	0.0008	-24.92	-30.29
450	1.02	15.97	0.4791	0.0020	-23.31	-28.69
500	1.02	20.71	0.6213	0.0034	-22.38	-27.76
550	1.025	47.57	1.4271	0.0069	-20.91	-26.28
525	1.021	16.56	0.4968	0.0080	-21.59	-26.96
475	2	4.430	0.1329	0.0084	-23.48	-28.86
425	2	0.6883	0.0206	0.0084	-25.32	-30.70
450	2	1.730	0.0519	0.0085	-24.39	-29.77
500	1.02	5.439	0.1632	0.0089	-22.54	-27.92
550	1.03	37.34	1.1203	0.0116	-20.46	-25.84
600	1.075	202.35	6.0705	0.0262	-18.21	-23.58
650	1.047	292.68	8.7804	0.0472	-17.15	-22.52
625	1.063	86.30	2.5890	0.0534	-18.07	-23.44
575	1.03	17.49	0.5246	0.0547	-19.56	-24.94
502	9.99	6.570	0.1971	0.0551	-22.80	-28.17
525	1.01	6.005	0.1802	0.0556	-20.59	-25.96
555	1.03	8.560	0.2568	0.0562	-20.24	-25.62
585	1.07	20.53	0.6160	0.0577	-19.39	-24.76
630	1.06	71.91	2.1572	0.0628	-18.07	-23.44
650	1.07	106.1	3.1841	0.0705	-17.59	-22.96
610	1.08	30.37	0.9111	0.0726	-18.78	-24.15
570	2.02	15.47	0.4640	0.0738	-20.05	-25.43
530	3	6.481	0.1944	0.0742	-21.31	-26.68
490	4	2.278	0.0684	0.0744	-22.64	-28.01
550	1.025	4.313	0.1294	0.0747	-20.63	-26.01
600	1.08	20.89	0.6267	0.0762	-19.10	-24.47
649	1.05	72.02	2.1607	0.0814	-17.79	-23.16
675	1.04	131.1	3.9334	0.0908	-17.09	-22.47
700	1	179.5	5.3847	0.1037	-16.53	-21.91
750	1	415.8	12.4754	0.1336	-15.48	-20.85
725	1.01	165.6	4.9675	0.1455	-16.23	-21.60
675	1.01	41.58	1.2474	0.1485	-17.55	-22.93
625	1.03	10.36	0.3109	0.1492	-18.94	-24.32
575	2.06	4.235	0.1270	0.1495	-20.53	-25.90

625	1.03	18.00	0.5401	0.1508	-18.38	-23.76
800	1.046	500.4	15.0111	0.1868	-14.94	-20.31
800	1.032	294.8	8.8427	0.2080	-15.27	-20.65
800	3.09	594.6	17.8376	0.2507	-15.48	-20.86
	Fusion	10422	312.6653	1.0000		

CIT-2048 D5
Equivalent sphere radius of 294 µm

Temp (C)	Time (hr)	^{3}He (10^{-18} mol)	± σ	^{C}F	$\ln(D/a^2)$	ln(D)
300	1.04	2.29	0.07	0.0002	-27.36	-34.41
350	1.02	5.43	0.16	0.0008	-25.00	-32.05
400	1.02	14.57	0.44	0.0023	-22.91	-29.97
450	1.03	28.50	0.86	0.0053	-21.36	-28.42
500	1.04	30.42	0.91	0.0084	-20.72	-27.77
550	1.05	105.0	3.15	0.0193	-18.78	-25.83
525	1.04	34.68	1.04	0.0229	-19.46	-26.51
475	2.02	9.08	0.27	0.0239	-21.36	-28.41
425	2.04	1.36	0.04	0.0240	-23.25	-30.30
450	2.02	3.21	0.10	0.0243	-22.37	-29.42
500	1.04	10.33	0.31	0.0254	-20.51	-27.56
550	1.05	74.16	2.22	0.0331	-18.38	-25.44
600	1.02	353.7	10.61	0.0698	-16.23	-23.28
650	1.02	550.3	16.51	0.1269	-15.05	-22.11
625	1.01	155.8	4.67	0.1431	-15.96	-23.01
575	1.05	30.54	0.92	0.1462	-17.55	-24.60
525	2.04	11.26	0.34	0.1474	-19.19	-26.25
525	2.02	10.46	0.31	0.1485	-19.25	-26.30
525	2.02	11.52	0.35	0.1497	-19.14	-26.20
555	1.03	15.25	0.46	0.1513	-18.18	-25.23
580	1.055	31.24	0.94	0.1545	-17.47	-24.52
605	1.02	63.45	1.90	0.1611	-16.69	-23.74
630	1.01	120.9	3.63	0.1736	-15.97	-23.02
655	1.017	207.3	6.22	0.1952	-15.32	-22.37
700	1.047	501.0	15.03	0.2472	-14.25	-21.30
750	1.06	850.6	25.52	0.3354	-13.38	-20.43
800	1.06	1145	34.35	0.4542	-12.65	-19.71
850	1.06	1383	41.49	0.5977	-11.99	-19.04
850	2.04	1194	35.82	0.7217	-12.30	-19.35
	fusion	2682	80.47	1.0000		

CIT-2048 D10
Equivalent sphere radius of 425 um

Temp (C)	Time (hr)	^{3}He (10^{-18} mol)	± σ	^{C}F	ln(D/a^2)	ln(D)
uncertain	1	4.719	0.1416	0.0023	NA	NA
uncertain	1	6.453	0.1936	0.0055	NA	NA
496	1	4.272	0.1282	0.0075	-21.14	-27.46
500	1	2.731	0.0819	0.0089	-21.36	-27.67
490	0.5	0.701	0.0210	0.0092	-21.93	-28.24
480	1	0.876	0.0263	0.0096	-22.36	-28.67
470	1	0.663	0.0199	0.0100	-22.60	-28.91
460	2	0.987	0.0296	0.0104	-22.85	-29.17
450	3	1.291	0.0387	0.0111	-22.93	-29.25
440	4	1.340	0.0402	0.0117	-23.13	-29.44
430	5	0.709	0.0213	0.0121	-23.94	-30.26
420	6	1.007	0.0302	0.0126	-23.74	-30.06
410	7	0.844	0.0253	0.0130	-24.03	-30.35
400	8	0.858	0.0257	0.0134	-24.12	-30.44
405	8	0.900	0.0270	0.0138	-24.04	-30.36
415	7	1.076	0.0323	0.0144	-23.69	-30.01
425	6	1.086	0.0326	0.0149	-23.49	-29.81
435	5	1.678	0.0503	0.0157	-22.83	-29.15
445	4	1.420	0.0426	0.0164	-22.73	-29.04
455	3	1.888	0.0566	0.0173	-22.10	-28.42
465	2	1.626	0.0488	0.0181	-21.80	-28.12
475	1	1.309	0.0393	0.0188	-21.28	-27.60
485	1	1.431	0.0429	0.0195	-21.16	-27.47
495	1	2.128	0.0638	0.0205	-20.72	-27.03
500	1	2.451	0.0735	0.0217	-20.52	-26.84
500	1	2.187	0.0656	0.0228	-20.58	-26.90
500	1	2.602	0.0781	0.0240	-20.36	-26.67
500	1	2.178	0.0654	0.0251	-20.49	-26.80
500	1	2.390	0.0717	0.0263	-20.35	-26.67
520	1	4.481	0.1344	0.0285	-19.66	-25.97
500	1	2.040	0.0612	0.0294	-20.39	-26.71
480	1	0.979	0.0294	0.0299	-21.10	-27.41
460	2	0.832	0.0250	0.0303	-21.94	-28.26
440	4	0.776	0.0233	0.0307	-22.69	-29.01
450	3	0.652	0.0195	0.0310	-22.56	-28.88
475	1	0.737	0.0221	0.0314	-21.33	-27.65
500	1	2.192	0.0658	0.0325	-20.22	-26.54

Final	1982	59.46	1